



Dual-lasing channel quantum cascade laser based on scattering-assisted injection design

BOYU WEN,^{1,2} CHAO XU,¹ SIYI WANG,¹ KAIXI WANG,¹ MAN CHUN TAM,¹
ZBIG WASILEWSKI,¹ AND DAYAN BAN^{1,3}

¹Department of Electrical and Computer Engineering, Waterloo Institute for Nanotechnology,
University of Waterloo, 200 University Ave W. Waterloo, Ontario N2L 3G1, Canada

²b4wen@uwaterloo.ca

³dban@uwaterloo.ca

Abstract: A dual lasing channel Terahertz Quantum Cascade laser (THz QCL) based on GaAs/Al_{0.17}Ga_{0.83}As material system is demonstrated. The device shows the lowest reported threshold current density (550A/cm² at 50K) of GaAs/Al_xGa_{1-x}As material system based scattering-assisted (SA) structures and operates up to a maximum lasing temperature of 144K. Dual lasing channel operation is investigated theoretically and experimentally. The combination of low frequency emission, dual lasing channel operation, low lasing threshold current density and high temperature performance make such devices ideal candidates for low frequency applications, and initiates the design strategy for achieving high-temperature performance terahertz quantum cascade laser with wide frequency coverage at low frequency.

© 2018 Optical Society of America under the terms of the [OSA Open Access Publishing Agreement](#)

OCIS codes: (140.5965) Semiconductor lasers, quantum cascade; (140.3070) Infrared and far-infrared lasers.

References and links

1. S. S. Dhillon, M. S. Vitiello, E. H. Linfield, A. G. Davies, M. C. Hoffmann, J. Booske, C. Paoloni, M. Gensch, P. Weightman, G. P. Williams, E. Castro-Camus, D. R. S. Cumming, F. Simoons, I. Escorcia-Carranza, J. Grant, S. Lucyszyn, M. Kuwata-Gonokami, K. Konishi, M. Koch, C. A. Schmuttenmaer, T. L. Cocker, R. Huber, A. G. Markelz, Z. D. Taylor, V. P. Wallace, J. Axel Zeitler, J. Sibik, T. M. Korter, B. Ellison, S. Rea, P. Goldsmith, K. B. Cooper, R. Appleby, D. Pardo, P. G. Huggard, V. Krozer, H. Shams, M. Fice, C. Renaud, A. Seeds, A. Stöhr, M. Naftaly, N. Ridler, R. Clarke, J. E. Cunningham, and M. B. Johnston, "The 2017 terahertz science and technology roadmap," *J. Phys. D Appl. Phys.* **50**(4), 043001 (2017).
2. G. Liang, L. Tao, and Q. Wang, "Recent developments of terahertz quantum cascade lasers," *IEEE J. Sel. Top. Quantum Electron.* **23**(4), 1–18 (2017).
3. M. A. Belkin and F. Capasso, "New frontiers in quantum cascade lasers: high performance room temperature terahertz sources," *Phys. Scr.* **90**(11), 118002 (2015).
4. A. Valavanis, J. Zhu, J. Freeman, L. Li, L. Chen, A. G. Davies, E. H. Linfield, and P. Dean, "Terahertz quantum cascade lasers with >1 W output powers," *Electron. Lett.* **50**(4), 309–311 (2014).
5. S. Fatholouloumi, E. Dupont, C. W. I. Chan, Z. R. Wasilewski, S. R. Laframboise, D. Ban, A. Mátyás, C. Jirauschek, Q. Hu, and H. C. Liu, "Terahertz quantum cascade lasers operating up to ~ 200 K with optimized oscillator strength and improved injection tunneling," *Opt. Express* **20**(4), 3866–3876 (2012).
6. X. Yang, X. Zhao, K. Yang, Y. Liu, Y. Liu, W. Fu, and Y. Luo, "Biomedical applications of terahertz spectroscopy and imaging," *Trends Biotechnol.* **34**(10), 810–824 (2016).
7. M. Röscher, G. Scalari, M. Beck, and J. Faist, "Octave-spanning semiconductor laser," *Nat. Photonics* **9**(1), 42–47 (2015).
8. Y. Yang, D. Burghoff, J. Reno, and Q. Hu, "Achieving comb formation over the entire lasing range of quantum cascade lasers," *Opt. Lett.* **42**(19), 3888–3891 (2017).
9. S. Khanal, L. Gao, L. Zhao, J. L. Reno, and S. Kumar, "High-temperature operation of broadband bidirectional terahertz quantum-cascade lasers," *Sci. Rep.* **6**(1), 32978 (2016).
10. S. Kumar, C. W. I. Chan, Q. Hu, and J. L. Reno, "A 1.8-THz quantum cascade laser operating significantly above the temperature of $\hbar\Omega/k_B$," *Nat. Photonics* **7**(2), 166–171 (2011).
11. E. Dupont, S. Fatholouloumi, Z. R. Wasilewski, G. Aers, S. R. Laframboise, M. Lindsog, S. G. Razavipour, A. Wacker, D. Ban, and H. C. Liu, "A phonon scattering assisted injection and extraction based terahertz quantum cascade laser," *J. Appl. Phys.* **111**(7), 073111 (2012).
12. S. G. Razavipour, E. Dupont, S. Fatholouloumi, C. W. I. Chan, M. Lindsog, Z. R. Wasilewski, G. Aers, S. R. Laframboise, A. Wacker, Q. Hu, D. Ban, and H. C. Liu, "An indirectly pumped terahertz quantum cascade laser with low injection coupling strength operating above 150 K," *J. Appl. Phys.* **113**(20), 203107 (2013).

13. S. G. Razavipour, E. Dupont, C. W. I. Chan, C. Xu, Z. R. Wasilewski, S. R. Laframboise, Q. Hu, and D. Ban, "A high carrier injection terahertz quantum cascade laser based on indirectly pumped scheme," *Appl. Phys. Lett.* **104**(4), 041111 (2014).
14. S. Khanal, J. L. Reno, and S. Kumar, "2.1 THz quantum-cascade laser operating up to 144 K based on a scattering-assisted injection design," *Opt. Express* **23**(15), 19689–19697 (2015).
15. H. Yasuda, T. Kubis, P. Vogl, N. Sekine, I. Hosako, and K. Hirakawa, "Nonequilibrium Green's function calculation for four-level scheme terahertz quantum cascade lasers," *Appl. Phys. Lett.* **94**(15), 151109 (2009).
16. B. S. Williams, H. Callebaut, S. Kumar, Q. Hu, and J. L. Reno, "3.4-THz quantum cascade laser based on longitudinal-optical-phonon scattering for depopulation," *Appl. Phys. Lett.* **82**(7), 1015–1017 (2003).
17. Y. V. Flores and A. Albo, "Impact of Interface Roughness Scattering on the Performance of GaAs/Al_xGa_{1-x}As Terahertz Quantum Cascade Lasers-erratum," *IEEE J. Quantum Electron.* **53**(5), 1 (2017).
18. Y. V. Flores and A. Albo, "Impact of interface roughness scattering on the performance of GaAs/Al_xGa_{1-x}As terahertz quantum cascade lasers," *IEEE J. Quantum Electron.* **53**(3), 1–8 (2017).
19. H. Yasuda, "Intervalley scattering in terahertz quantum cascade lasers with GaSb and InGaSb wells," *AIP Adv.* **8**(2), 025125 (2018).
20. K. Leosson, J. R. Jensen, W. Langbein, and J. M. Hvam, "Exciton localization and interface roughness in growth-interrupted GaAs/AlAs quantum wells," *Phys. Rev. B* **61**(15), 10322–10329 (2000).
21. S. G. Razavipour, "Design, Analysis, and Characterization of Indirectly-pumped Terahertz Quantum Cascade Lasers," PhD thesis, University of Waterloo, Department of Electrical and Engineering (2013).
22. S. V. Meshkov, "Tunneling of electrons from a two-dimensional channel into the bulk," *Zh. Eksp. Teor. Fiz.* **91**(2252), 198 (1986).
23. H. Schneider and H. C. Liu, *Quantum well infrared photodetectors* (Springer, 2007), Chap. 4.
24. B. F. Levine, C. G. Bethea, G. Hasnain, V. O. Shen, E. Pelve, R. R. Abbott, and S. J. Hsieh, "High sensitivity low dark current 10 μ m GaAs quantum well infrared photodetectors," *Appl. Phys. Lett.* **56**(9), 851–853 (1990).
25. J. S. Blakemore, "Semiconducting and other major properties of gallium arsenide," *J. Appl. Phys.* **53**(10), R123–R181 (1982).
26. R. Quay, C. Moglestue, V. Palankovski, and S. Selberherr, "A Temperature Dependent Model for the Saturation Velocity in Semiconductor Materials," *Mater. Sci. Semicond. Process.* **3**(1–2), 149–155 (2000).
27. C. Xu, "Toward High Performance Broad-band Frequency Comb Operation of Terahertz Quantum Cascade Lasers," PhD thesis, University of Waterloo, Department of Electrical and Engineering (2017).
28. C. Xu, S. G. Razavipour, Z. Wasilewski, and D. Ban, "An investigation on optimum ridge width and exposed side strips width of terahertz quantum cascade lasers with metal-metal waveguides," *Opt. Express* **21**(26), 31951–31959 (2013).
29. A. Albo and Q. Hu, "Investigating temperature degradation in THz quantum cascade lasers by examination of temperature dependence of output power," *Appl. Phys. Lett.* **106**(13), 131108 (2015).

1. Introduction

Terahertz (THz) gap, which is often defined as an electromagnetic (EM) wave frequency range from 0.3 to 10 THz, has great potential for applications such as non-destructive imaging, spectroscopic identification of chemical and biological species and ultra-high speed communication [1,2]. However, electromagnetic waves at the terahertz band remains relatively underexploited comparing to microwave and mid-infrared frequencies due to the lack of compact, efficient and broadband radiation sources [1,2].

Terahertz Quantum Cascade Laser has been recognized as one of the most promising coherent radiation sources in this EM band since its inception. To date, THz QCLs can cover a wide frequency range of ~1-5 THz [3] and produce watt-level output power in pulse mode [4]. Although THz QCLs have been used in some practical applications, technical difficulties, such as cryogenic operating temperature [5] and poorer performance at lower frequencies (<2.5THz) [3], prevent further and wider deployment of this device technology. As the characteristic absorption of many biomolecules is located in the THz range, largely at frequencies below 2.5 THz [6], it is of scientific interest and technological importance to develop THz QCLs at those frequencies. Broadband emission is another challenge that remains to be addressed, which is not only essential for the biomolecular terahertz spectroscopy but also critical for other applications such as frequency comb operation and tunable THz emission sources [7,8]. Bound to continuum-based quantum designs are most commonly used for broadband terahertz emission. However, the broadband gain in the bound to continuum (BTC) structures is achieved often at the expense of device operating temperature performance. As a result, BTC-based THz QCLs can lase only at lower temperatures compared to their counterparts based on resonant phonon (RP) or scattering-

assisted designs at the similar frequencies [3]. Bidirectional THz QCL is another option to achieve broadband emission – light emission at different terahertz frequencies was observed when the device bias polarity was switched [9]. Dual color emission operation under the same device bias polarity was also observed when the devices were biased at different voltages. The THz QCL in [10] first lased at ~ 4 THz at a lower bias (a lower current injection), then at ~ 1.8 THz at a higher bias, which was attributed to the sequential turn-on of two different lasing transition channels. There is a substantial spectral gap ($4 - 1.8 = 2.2$ THz) between the two lasing frequencies.

In this paper, four-well GaAs/Al_{0.17}Ga_{0.83}As THz QCLs based on the scattering-assisted scheme that can lase up to 144 K is developed and demonstrated. The Al composition of the AlGaAs barriers is 17%, providing better suppression for leakage current to continuum band at higher temperatures, which is evidenced by lower threshold current density. A large injection coupling strength (1.7 meV) is adopted. Numerical simulations predict that two lasing channels contribute to device optical gain, which is supported by experimental results. The devices exhibit lasing emission spectra covering 2.3-2.6 THz and a large dynamic range from ~ 550 to over ~ 825 A/cm² (at 20K). The study shows that a THz QCL quantum design allowing two lasing channels may be a promising approach to achieve wide frequency coverage, low threshold current density and good device performance at low frequency (~ 2.5 THz). Compared to the device reported in [14] that emits light in similar frequency, a 26% lower threshold current density, wider frequency coverage (0.3THz to 0.13THz) and the same maximum operation temperature are achieved. A summary of previous scattering-assisted structures with top temperature performance is shown in Table 1.

Table 1. Scattering-assisted based THz QCL structure key parameters and performance summary.

Design	Material System	Main frequency	T _{max}	Current Density (heatsink temperature)	Injection coupling strength $\hbar\Omega$	Oscillator strength
Kumar et al. [10]	GaAs/Al _{0.15} Ga _{0.85} As	1.8THz and 4THz	163K	865 A/cm ² (10K)	0.75meV	0.6
Dupont et al. [11]	GaAs/Al _{0.25} Ga _{0.75} As	3.2THz	138K	1170 A/cm ² (10K)	1.14meV	0.39
Razavipour et al. [12]	GaAs/Al _{0.25} Ga _{0.75} As	2.4THz	153K	800 A/cm ² (10K)	0.845meV	0.27
Razavipour et al. [13]	GaAs/Al _{0.25} Ga _{0.75} As	2.67THz	151K	1440 A/cm ² (10k)	1.54meV	0.27
Khanal et al. [14]	GaAs/Al _{0.15} Ga _{0.85} As	2.1THz	144K	745 A/cm ² (46K)	~ 1.55 meV	0.39
This Work	GaAs/Al _{0.17} Ga _{0.83} As	2.4THz	144K	550 A/cm ² (50K)	1.7meV	0.44 and 0.27

2. THz QCL design and simulation

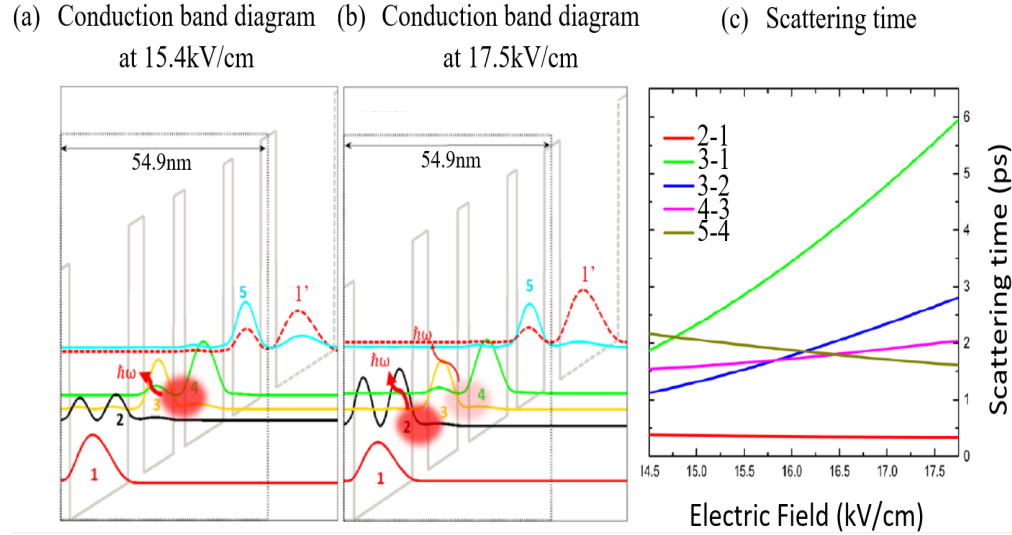


Fig. 1. Conduction band diagram at Electric Field of 15.4 kV/cm (a) and 17.5 kV/cm (b). (c) Simulation of scattering time between states 3-1 (green), states 2-1 (red), states 3-2 (blue), states 5-4 (brown) and states 4-3 (pink) versus electric field at 30K.

Scattering-assisted design schemes show the best temperature performance at low frequency (<2.5 THz) because of its efficient and selective charge carrier injection [3,15]. At low frequencies, the energy spacing (~10 meV) between lasing states are comparable to the energy broadening (~4 meV) [16], selectively injecting carriers to the upper lasing state rather than the lower lasing state becomes more challenging [14]. In order to sustain higher population inversion to achieve high optical gain for wide frequency coverage, a GaAs/Al_{0.17}Ga_{0.83}As quantum design based on scattering-assisted pumping scheme is adopted. Each module consists four quantum wells and four barrier layers, the actual layer thickness extracted from high-resolution X-ray diffraction (HRXRD) measurement, in angstrom are **40.3/79.7/29.7/103.6/24.1/74.4/40.3/156.7**, starting from the rightmost barrier in the period (shown in Fig. 1) with barriers indicated in bold fonts and doped layer underlined. The widest well is n-doped with Si at $2.02 \times 10^{16} \text{ cm}^{-3}$, and average sheet doping density in one module is $3.17 \times 10^{10} \text{ cm}^{-2}$.

The conduction band diagrams at electric fields of 15.4 and 17.5 kV/cm are shown in Fig. 1(a) and 1(b), respectively, together with the energy levels and the square of their corresponding wavefunctions. In one module, carrier transport and potential optical transitions basically involve the five lowest quantum states (1-5). The state 5 is highly coupled with state 1' from the previous module for effective electron inter-module transport. Population inversion can potentially be built up between the states 4 and 3 and between the states 3 and 2, yielding two stimulated emission transitions, as denoted in Fig. 1.

The state 5 is located ~30.3 meV-32.7 meV above the state 4 at electric fields from 15.4 to 17.5 kV/cm. Though this energy separation is slightly less than GaAs longitudinal-optical (LO) phonon energy (36 meV), the electron-LO phonon scattering from the states 5 to 4 is adequately efficient [11, 12]. As shown in Fig. 1(c), the calculated scattering time τ_{54} is below 2.5 ps in this electric field range and decreases as the increasing of the electric field. The scattering times for other transitions (τ_{21} , τ_{42} , τ_{32} , τ_{43}) are also plotted in Fig. 1(c). The states 3 and 2 are aligned at an electric field of 12.4 kV/cm, while the state 1' aligns with the state 5 at 15.4 kV/cm. At a lower bias (~15 kV/cm), the state 3 is depopulated via scattering and resonant tunneling to the state 2 (only semi-classical scattering is included in Fig. 1(c)), and

electron population inversion is achieved between states 4 and 3. This yields the first stimulated optical transition (so-called the first lasing channel thereafter). Simulation shows that lasing frequency of subbands 4-3 is 2.27THz (9.4meV) at 15.4kV/cm. While the applied electric field is increased to 17.5 kV/cm, the states 3 and 2 become misaligned and the electron transport from 3 to 2 is significantly slowed down. As shown in Fig. 1(c), τ_{32} increases from ~ 1 ps at 14.5 kV/cm to ~ 3 ps at 17.75 kV/cm in Fig. 1(c). Nevertheless, state 3 continues to be populated directly from the state 4 via nonradiative scattering or stimulation emission transition or even directly from the state 5 via LO phonon scattering (τ_{53} is in 6ps to 9ps range which is not shown). In particular, τ_{32} exceeds τ_{43} beyond the electric field of ~ 15.8 kV/cm. Electrons are therefore accumulated at the state 3 and population inversion is built up between the states 3 and 2, yielding the second stimulated optical transition (the second lasing channel). Electrons at the state 2 can be quickly depopulated via fast LO phonon scattering to the ground state 1 as τ_{21} remains very short at ~ 0.4 ps over the whole electric field range of interest.

There are several key parameter differences between this device and previous scattering-assisted based structure. Firstly, energy spacing between state 4 and 5 changes from 30.3meV to 32.7meV from electric field of 15.4kV/cm to 17.5kV/cm. This energy spacing is closer to phonon energy compare to [10], so that high frequency radiative emission between subbands 5 and 4 is prevented. Secondly, barriers of $\text{Al}_{0.17}\text{Ga}_{0.83}\text{As}$ are adopted, the barrier height (154meV) is tuned to be lower than [11–13], but higher than those in [10,14]. This choice is a trade-off for reducing interface roughness while effectively suppressing carrier leakage into continuum band. In [14], S. Khanal et al. have proved that scattering-assisted design can be utilized with low barrier material system ($\text{Al}_{0.15}\text{Ga}_{0.85}\text{As}/\text{GaAs}$), and low threshold current density of 745A/cm² has been achieved due to lower interface roughness scattering. However, it is arguable that device in Ref.14 is damaged by leakage to continuum which is supported by the absence of negative differential resistance (NDR) at even 46K. A tradeoff between interface roughness scattering and leakage to continuum has been pointed out in [17,18]. A numerical simulation for the device reported in this paper shows that increasing barrier height from 15% Al to 17% Al will reduce leakage current to continuum from 418A/cm² to 204A/cm², while interface roughness scattering time between state 4 and 3 decreases from 3.05ps to 2.53ps. A further increased barrier height may result even less leakage to continuum, but it is on risk to make interface roughness scattering faster than LO phonon scattering (~ 2.4 ps at 160K) as another dominant scattering mechanism as shown in Table 2. The three parameters are calculated when barrier height is the only variable. In order to reduce threshold current density without introducing too much interface roughness scattering, a barrier height of 17% Al is decided for this structure. Thirdly, High injection coupling strength was chosen to maintain high optical gain peak value. The coupling energy ($\hbar\Omega_{15}$) is 1.7 meV. This is higher than the other scattering-assisted designs based on the same material system, as summarized in Table 1. Finally, the alignment of state 3-2 is detuned to lower electric field than state 5-1' aligns, and the energy spacing between states 3 and 2 increased to ~ 9.9 meV at 17.5kV/cm for the second lasing channel operation.

Table 2. Interface roughness scattering, LO phonon scattering and leakage to continuum calculation for different barrier height at lattice temperature of 160K and applied electric field of 15.5kV/cm.

	15%Al	17%Al	19%Al
Interface roughness scattering between state 4 and 3 (ps)	3.05	2.53	2.16
LO phonon scattering between state 4 and 3 (ps)	2.34	2.39	2.46
Leakage to continuum (A/cm ²)	418	204	101

The theoretical modeling of non-lasing device is based on a rate equation approach, as it is proved to be reliable for simulating THz QCLs based on a scattering-assisted pumping scheme [12,13]. Tight binding method is applied only between modules, and all transition

within one module is treated semi-classically, because 3-2 is not perfectly aligned at design bias and electron transports between state 1' and state 5 via effective tunneling at design bias. interface roughness, LO phonon, and impurity scattering have been included in intersubband scattering, the electron distribution on each energy levels is considered obeying Fermi-Dirac distribution. When calculating the interface roughness scattering, the mean height of roughness and the correlation length are 4Å and 128Å, respectively, and the product of these two values is similar to the product of values used in [19] for GaAs/AlGaAs based QCL. The interface roughness may vary between different growth conditions. The typical experimental values of correlation length ranges from 6nm to 15nm, and roughness height varies around 2 monolayers [20]. The used parameters are estimated in this range. The current density – voltage (J-V) curve calculation is based on second order rate equation which includes the effect of carrier thermal distribution in different states on charge carrier tunneling [21]. Electron temperature is set to be 90K above the heat sink temperature.

The leakage to continuum was calculated by obtaining electron density that has ability to escape to continuum. Electrons density on each subbands with energy above the barrier edge are included by Eq. (1):

$$N_{2D} \approx \frac{m}{\pi \hbar^2} k_B T \exp\left(\frac{-E_{act}}{k_B T}\right), \quad (1)$$

where E_{act} is the thermal activation energy which equals the energy difference between the barrier edge and the Fermi level in the each subbands that are calculating. Additionally, electrons with energy lower than barrier edge may also be able to scatter into the energy levels are slightly lower than barrier edges, and tunnel into continuum. Hence, electrons with lower thermal energy than activation energy are also considered to have possibility to escape to continuum via scattering-assisted tunneling [22,23], and it can be calculated in Eq. (2) [24]:

$$N_{2DLE} = \int_{E_1}^{E_b} \frac{m}{\pi \hbar^2} T(E, F) [1 + \exp\left(\frac{E - E_f}{K_B T}\right)]^{-1} dE, \quad (2)$$

where

$$T(E, F) = \exp\left[-2 \int_0^{Z_c} dz \sqrt{2m_b(E_b - E - eFz)} / \hbar\right] \quad (3)$$

is transmission coefficient, E_1 is electron energy that is lower than E_b (barrier edge energy), $Z_c = (E_b - E/eF)$ is classical turning point or barrier thickness that electron may tunnel through at the calculating energy, and F is applied electric field [23]. Finally, the leakage current can be calculated with formula [24]:

$$J = e \frac{(N_{2D} + N_{2DLE})}{L_p} v(F) \quad (4)$$

and

$$v(F) = \frac{\mu F}{[1 + (\mu F / v_{sat})^2]^{\frac{1}{2}}}, \quad (5)$$

where L_p is length of one module, $\mu \approx 12000 \text{ cm}^2 \text{Vs}^{-1}$ is the mobility and $v_{sat} \approx 0.72 \times 10^7 \text{ cm}\cdot\text{s}^{-1}$ is saturated drift velocity [25,26].

3. Experiments

The quantum structure presented in Fig. 1 was grown on a semi-insulating GaAs substrate by using molecular beam epitaxy with 172 repeating modules in its 10 μm thick active region core. The widest well in each module is uniformly doped to achieve a sheet doping density of $3.17 \times 10^{10} \text{ cm}^{-2}$ per module. The active region is sandwiched between a 100 angstrom undoped GaAs spacer followed by a $100\text{nm}/5 \times 10^{18} \text{ cm}^{-3}$ n + GaAs and a 100 angstrom undoped GaAs spacer followed by a top stack of $5 \times 10^{18} \text{ cm}^{-3} / 5 \times 10^{19} \text{ cm}^{-3}$ (50nm/10nm) n + GaAs layers and capped with a 3.5nm low temperature growth GaAs layer.

The laser devices are processed with the conventional In-Au wafer bonding and with a Ti/Au double metal ridge waveguide [27]. The laser ridge is 150 μm wide and cleaved into 2.22 mm long. The measured maximum lasing temperature of the fabricated devices is 144 K, which is the same as reference device in [14]. The fabricated device also shows low threshold current density of 550 A/cm^2 at 50K. To eliminate high order mode competition in a wide ridge waveguide, which often yield kinks on measured light-current curves of THz QCLs [28], there are two 6.5 μm wide side strips of the n-GaAs contact layer uncovered by the top metal along the ridge waveguide of the devices, and n-GaAs layer is not etched. In other words, n⁺ doped top contact layer between the top metal and active region at the laser ridge waveguide edges is uncovered by top metal. High order optical modes will suffer from higher loss at the sides of ridge, while the fundamental optical mode mostly locates in the center of laser ridge and remains unaffected. Thus, the fundamental optical mode will dominate the output [28].

4. Results and discussions

Light (L)-current density (J) characteristics of the fabricated device from 20 to 130 K in pulse mode, with pulse frequency of 500Hz and pulse width of 500 ns, is shown in Fig. 2. The measured L-J curves at temperatures below 120K exhibit a substantial slump in optical output power between two peaks before reaching the negative differential resistance (NDR) point. Correspondingly, a turning point in the slope of the voltage (V) – current density (J) curve at 40 K is observed right after the first optical output peak, denoted by a dashed line in Fig. 2. A clear NDR is measured at high bias on Voltage-Current density curve, and NDR is observed up to 120K, while the similar device in [14] didn't show a clear NDR at 46K. Observation of NDR region up to 120K and a 26% reduction on threshold current density together proved the improvement of 17% Al barrier on leakage current suppression. Considering a wider emission spectrum (0.3THz compare to 0.13THz) and the same maximum operation temperature, this device should have achieved larger population inversion.

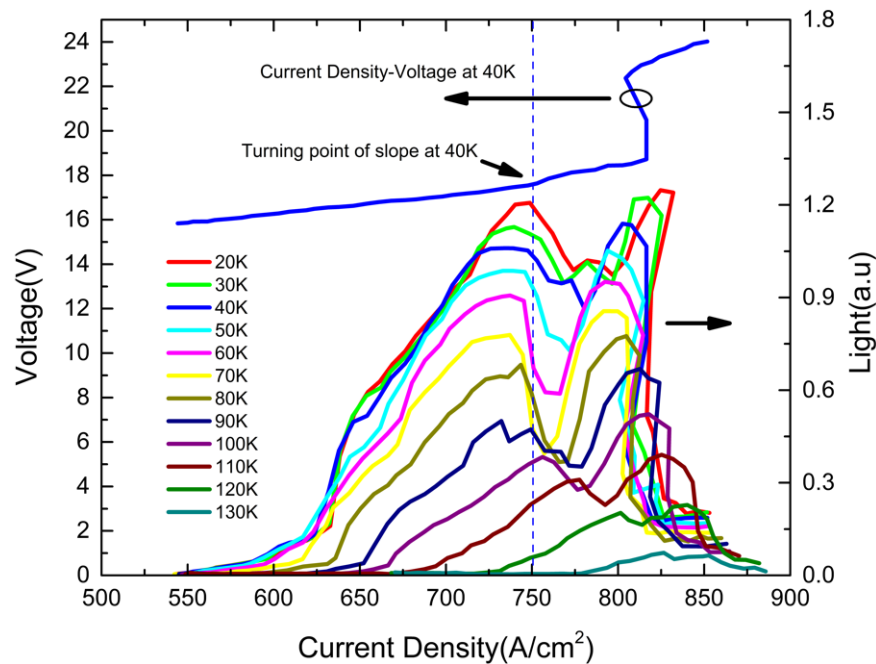


Fig. 2. Current Density-Voltage curve at 40K and Light-Current density curve after lasing threshold from 20K to 130K.

The experimental J-V curve is compared to the simulation results of a non-lasing structure, as shown in Fig. 3(a). After including the extra voltage drop (~ 1.2 V) due to the Schottky contact, the simulation and experimental curves are in good agreement. Three pre-threshold tunneling resonances are observed at device biases of 4.7 V (for 1'-4), 7.4 V (1'-3) and 8.9 V (1'-2), respectively, corresponding well with the two shoulders in the experimental curve. The measured threshold voltage at 90K is 16.1 V, as denoted by a dashed line in the Fig. 3(a). The device enters NDR region at ~ 19 V at 90K.

In order to understand the double peaks observed in the optical output power curve, the light-voltage (L-V) curve at 30 K is re-plotted in Fig. 3(b), shown together are the calculated optical gain peak values (in non-lasing case) as a function of device bias for the first (the 4-3 transition) and the second lasing channels (the 3-2 transition). The 4-3 transition peak gain reaches its maximum of 31.19 cm^{-1} at $\sim 15.7 \text{ kV/cm}$ with an oscillator strength of 0.44, while that of the 3-2 transition reaches 42.78 cm^{-1} at $\sim 17.5 \text{ kV/cm}$ with an oscillator strength of 0.27 at 30K. The first lasing channel is turned on first at low biases ($\sim 15.8 \text{ V}$, 14.6 kV/cm), leading to the ignition and increase of the lasing emission. The lasing emission is peaked around 17.3 V ($\sim 16.1 \text{ kV/cm}$), corresponding well to the bias at which the 4-3 transition optical gain (the red curve) is maximized. Beyond this bias, the states 3 and 2 become more and more misaligned and the fast resonant tunneling from 3 to 2 slows down. Charge carriers therefore pile up at state 3 and the population inversion between 4 and 3 is diminishing, leading to the quick reduction of the corresponding peak gain value. The shut-down of the first lasing channel contributes to the observed reduction in the lasing optical output power.

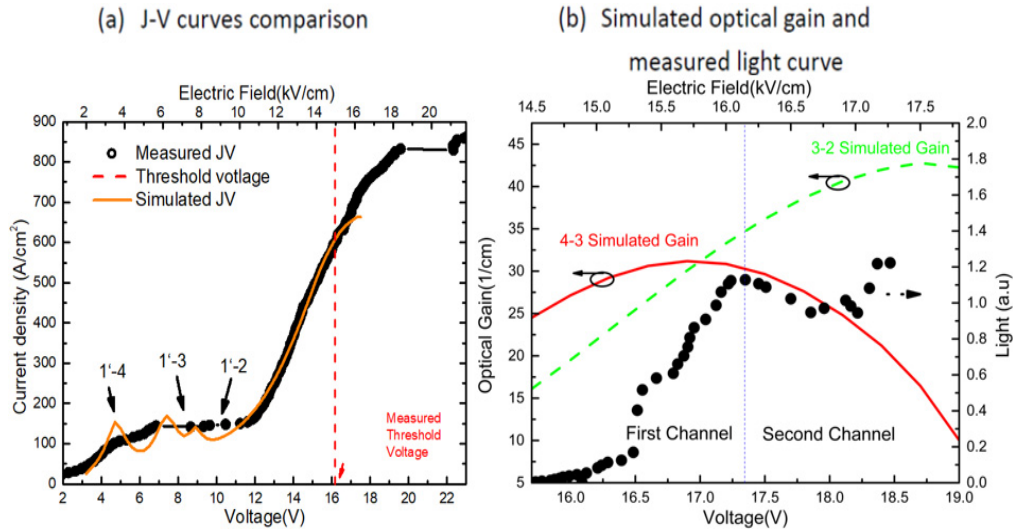


Fig. 3. (a) Simulated JV curve (orange solid line) in comparison with experimental IV curve at 90K (black circles). Schottky junction voltage drop of 1.2V is considered. (b) Simulated optical gain (non-lasing case) between states 4-3 (red) and 3-2 (green) in comparison between measured Light-Voltage curve (black dots) at 30K. A Schottky voltage drop of 1.2V is assumed. Two channels are distinguished by light curve, while the 4-3 transition dominates the first channel and switch to second channel while 4-3 optical gain becomes too weak.

The second lasing channel (the 3-2 transition) is turned on at higher biases. As the optical transitions from the 4-3 pair and the 3-2 pair do not overlap exactly in lasing frequency (to be shown in Fig. 5 shortly), the increase of the 3-2 transition peak gain is not necessarily compensating the reduction of the 4-3 transition peak gain at the 4-3 lasing frequency. As a result, the measured overall lasing emission power doesn't bounce back until a bias of ~17.8 V, at which the 3-2 transition gain is high enough to overcome the optical loss at its corresponding lasing frequency, and reaches its second peak at ~18.5 V (~17.3kV/cm), when the second lasing channel is fully opened up. And device enters NDR region immediately after 18.5V at 30K. This explains the double peak in the light-current density curves in Fig. 2.

The lasing channel switching is also indirectly manifested in the measured current density-voltage (J-V) curve. As the current-carrying capacity of the first lasing channel (4-3) is higher than that of the second one (3-2), the slope of the J-V curve in Fig. 2 exhibits a sudden change at the bias of ~17.58 V at 40K, marking the switching point of the dominant lasing channel transition.

To further reveal that the underlying mechanisms responsible for the two lasing emission peaks are different, the normalized peak value ($P_{out}(T)$) of the two optical emission peaks in the L-J curves of Fig. 2 is plotted as a function of $1/T$ in Fig. 4(a), where T is the temperature. For both peaks, the value of $P_{out}(T)$ decreases with the increase of T . An activation energy (E_a) can be extracted from high temperature end ($>90K$) by using equation $(1 - \frac{P_{out}}{P_{outmax}}) \approx \ln(a) - \frac{E_a}{K_B T}$ [29], where P_{outmax} is the maximum output power at the lowest temperature (20 K).

At low temperatures (below 113 K), the fitting to the emission peak curve from the first lasing channel (4-3) yields an activation energy $E_{a4-3} = 8.3$ meV, while the value is $E_{a3-2} = 18.4$ meV for the second lasing channel (3-2). The emission peak from the first lasing channel diminishes faster than that from the second lasing channel, and gradually becomes indistinguishable at temperatures higher than 120 K. The different activation energy derived from the fitting can be explained by the energy difference between the states 4 and 3. As described earlier, the first lasing emission peak (at lower biases) is mainly contributed from

the 4-3 transition where 4 is the upper lasing state (ULS) and 3 is the lower lasing state (LLS), while the second peak (at higher biases) from the 3-2 transition where 3 is the ULS and 2 is the LLS. At the design bias, an inter module leakage level (labeled as state 1) is ~ 5.4 meV above the first ULS(4) and ~ 15 meV above the second ULS (3) as shown in Fig. 4(b). Hence E_{a3-2} is ~ 10 meV larger than E_{a4-3} . Because of the lower activation energy, the 4-3 transition plays a substantial role only at lower temperatures (i.e., $< \sim 113$ K) and the 3-2 transition becomes more dominant at higher temperatures.

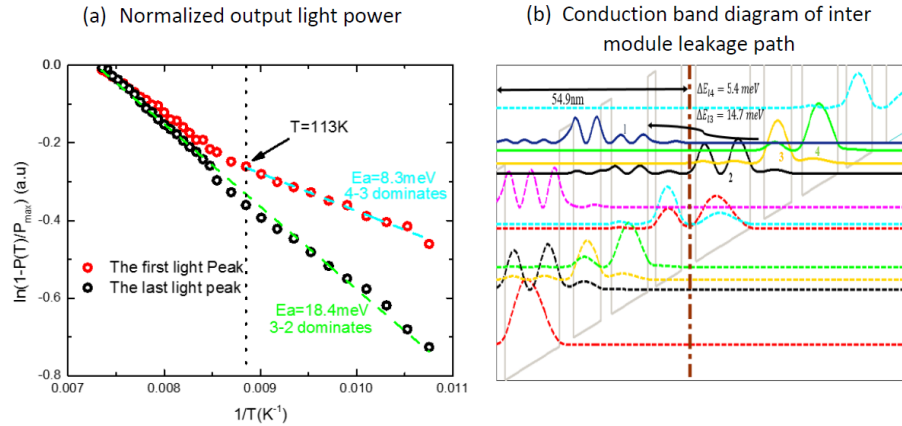


Fig. 4. (a) Normalized output light intensity of first peak (black dots) and second peak (red dots) in Light-Current curve versus temperature in plot of $\ln(1 - \frac{P_{out}(T)}{P_{outmax}})$ with fits (dashed lines).

Two peaks shows different trends until 113K. (b) Conduction band diagram shows possible inter module leakage path from states 4 and 3 to state 1. The energy spacing between states 4-1 and states 3-1 are 5.4 meV and 14.7 meV respectively.

The switching hypothesis of two lasing channels may be verified ultimately by measuring the lasing spectra at different device biases (current injection). Measured lasing spectra at different devices biases (16.5, 17.2, 18.2, 18.46 V) at 30K, and simulated gain spectra due to the 4-3 transition and the 3-2 transition under the corresponding conditions are presented together in Fig. 5. Optical gain is calculated in non-lasing case, and it is proportional to product of population inversion and oscillator strength. At the lower bias of 16.5 V, the lasing is observed at a frequency of ~ 2.3 THz, corresponding well with the peak frequency of the 4-3 transition gain spectrum (dashed red curve). As the device bias increases, the peak gain of the first lasing channel (4-3) diminishes. In addition, due to the Stark effect, the 4-3 transition peak frequency (marked by the brown solid squares at each bias) is almost linearly shifting to higher values (blue-shift, denoted by the brown solid line). The optical gain due to the second lasing channel (3-2) (dashed green line) starts to emerge on the lower frequency side at the bias of 17.2 V. As a result, the calculated overall gain (solid black line) exhibits a slower-paced blue shift. At higher biases such as 18.2 V and 18.4 V, the lasing spectra overlap well with the peak of the overall gain spectra, which is dominated by the optical gain contribution from the second lasing channel (3-2). The lasing spectra clearly demonstrate the transitions of two lasing channels during device operation. Due to the dual lasing channels, the lasing spectrum spans a range of $\sim 6.5\%$ of the central frequency of 2.35 THz at 1.317 Jth and 7.9% of the central frequency of 2.51 THz at 1.48 Jth. The frequency coverage is from 2.3 THz to 2.62 THz.

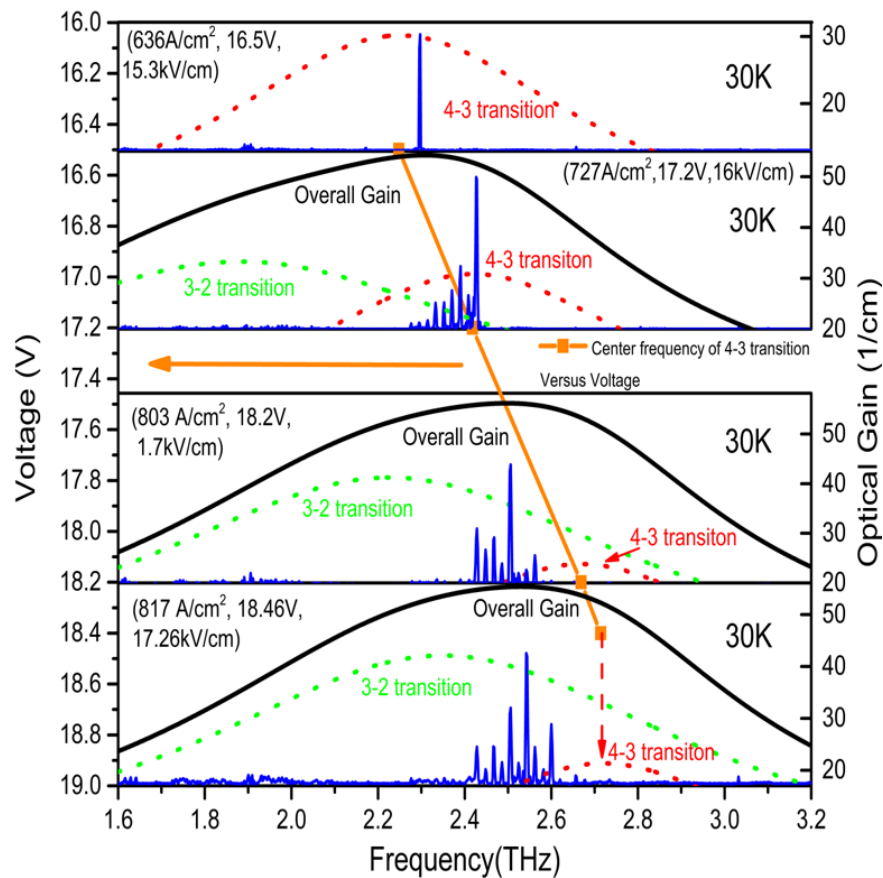


Fig. 5. Experimental lasing spectra (blue solid lines) in comparison with simulated optical gain of states 4-3 (red dashed line), states 3-2 (green dashed line) and total (black solid line) at 30K under different bias. The main center frequency of state 3-2 at different bias is labeled as red solid line to show contrast with experimental center frequency which is determined by total optical gain.

5. Conclusion

Here we presented a dual lasing channel QCL, which emits light from 2.3THz to 2.62THz at 30K, based on a scattering-assisted injection scheme in the GaAs/Al_{0.17}Ga_{0.83}As material system. The device shows a low threshold current density of 550A/cm² at 50K and maximum operating temperature of 144K. We proved that this dual lasing structure scheme can provide 0.3 THz frequency coverage at low frequency with the lowest reported threshold current density based on SA structures and a temperature performance close to the highest operating temperature recorded in this frequency range.

Funding

Natural Science and Engineering Research Council (NSERC); Ontario Research Foundation; Ontario Center of Excellence; University of Waterloo.

Acknowledgments

The authors would like to thank Dr. Seyed Ghasem Razavipour, Xiaoliang He and Yue Zhuo for technical assistance.